Multi-Modal Probes: Super-Resolution and TEM Imaging of Mitochondria, and Oxygen Mapping of Cells, Using Small-Molecule Ir(III) Luminescent Complexes

Jonathan R. Shewring,[a] Ahmet J. Cankut,[a] Luke K. McKenzie,[a] Bethany J. Crowston,[a] Stanley W. Botchway,[b] Julia A. Weinstein,[a] Elizabeth Edwards[*a] and Michael D. Ward*[*c].*

a Department of Chemistry, University of Sheffield, Sheffield S3 7HF, UK. E-mail: liz.edwards@sheffield.ac.uk

b Rutherford Appleton Laboratory, STFC Research Complex at Harwell, Harwell Science and Innovation Campus, Didcot OX11 0FA, UK

c Department of Chemistry, University of Warwick, Coventry CV4 7AL, UK

E-mail: m.d.ward@warwick.ac.uk

ABSTRACT. We describe an Ir(III)-based small molecule, multi-modal probe for use in both light and electron microscopy. Direct correlation of data between light-based and electron microscopy-based imaging to investigate cellular process at the ultrastructure level is a current challenge, requiring dyes which must be both brightly emissive for luminescence imaging, and scatter electrons to give contrast for EM, at a single working concentration suitable for both methods. Here we describe the use of Ir(III) complexes as probes that provide excellent image contrast and quality for both luminescence and electron microscopy imaging, *at the same working concentration*. Significant contrast enhancement of cellular mitochondria was observed in transmission electron imaging (TEM), with and without the use of typical contrast agents. The specificity for cellular mitochondria was also confirmed with MitoTracker® using confocal and 3D structured illumination microscopy (3D-SIM). These phosphorescent dyes are part of a very exclusive group of transition metal complexes that enable imaging beyond the diffraction limit. Triplet excited state phosphorescence was also utilized to probe O_2 concentration at the mitochondria *in-vitro*, using lifetime mapping techniques.

Introduction

Mitochondria play a pivotal role in mammalian cells, controlling a number of cellular processes such as metabolism, ATP generation, production of reactive oxygen species (ROS), cell death and Ca^{2+} homeostasis.[1] Mitochondrial function or "dysfunction" is also known to affect communication between cells and tissues, hence its emerging role in a number of neurodegenerative and metabolic diseases.[1] The microenvironment of mitochondria is closely related to their function, therefore the ability to measure local parameters such as pH, ROS concentration and O_2 concentration is essential to obtain a measure of cell health or disease progression. In particular the ability to monitor O_2 concentrations in mitochondria non-invasively and in real time is a significant target for the cell biology and microscopy communities, as O_2 is a key metabolite in the production of energy, as well as an important bio-marker for hypoxia and cancer detection.

Oxygen electrodes do offer a way of obtaining real-time measurements of $[O_2]$, however, this method is invasive and is not well suited to cell monolayers.[2-3] Immunostaining using Hypoxyprobe™ , an oxygen marker that binds only to cells that have oxygen saturation less than pO_2 of 10mm Hg at 37°C,[4] can also provide information on oxygen concentrations; but this is a static, end-point method of limited quantitative value. Electron paramagnetic resonance (EPR) spectroscopy has proved successful for monitoring $[O_2]$ *in vitro*,[5] however this requires more specialised user knowledge and equipment than other available techniques. A more user-friendly approach which has gained in popularity for O_2 monitoring (and pH sensing) is the use of luminescent probes which allow emission imaging. This approach provides a real-time, non-invasive method that can be conducted using a standard confocal microscope. For $[O_2]$ quantification, probes must undergo a change in emission intensity and lifetime on collision with

molecular O_2 which has a triplet ground state; this requires that the probe excited state also be a triplet, *i.e.* that the emission is phosphorescence. This provides that added advantage that lifetimes of phosphorescence are much longer than those of fluorescence, which makes changes in them potentially easier to detect.

Examples of such phosphorescent probes that have demonstrated promise for *in-situ* O_2 quantification are porphyrins [6-10] and transition metal complexes.[11-13] Their excited states are long-lived (τ = hundreds of nanoseconds to microseconds) due to the forbidden nature of the $T_1 \rightarrow S_0$ transition, which provides a large time window for collision with and quantification of O_2. As such, there have been a growing number of reports demonstrating *in vitro* O_2 sensing using single and two-photon lifetime imaging techniques (PLIM, PLM).[14-16] For example, these lifetime mapping techniques have been utilised in quantification of O_2 in 2D cell cultures, 3D spheroids and neurospheres using Pt(II) porphyrins.[8,17] Large dendritic Pt(II) porphyrins, which do not cross cellular membranes, have also been used to monitor O_2 levels in cerebral blood vessels of a living animal, using a bespoke two-photon phosphorescence lifetime imaging set-up.[9,18] Ratiometric probes, in which a dual emissive species acts as both calibrant and O_2 detector, have also been investigated for O_2 quantification.[19-20] These systems tend to utilize simpler instrumentation replying on emission intensity measurements, rather than lifetime mapping.

The challenge now is to utilize accumulated knowledge about how transition metal complex design affects cellular localisation and photophysical attributes, in order to create new probes that demonstrate organelle specificity and monitor O_2 concentration quantitatively. To do this we need probes that:

(i) can cross cellular membranes, without the use of permeabilisation detergents;

(ii) localise specifically at the cellular mitochondria, without perturbing their function;

(iii) have a luminescent triplet excited state with a high quantum yield and a long lifetime ($\sim 10^{-7}$ to 10^{-6} sec);

(iv) exhibit high sensitivity (high Stern-Volmer quenching constants) to O_2 at physiological concentrations.

O_2 detection with transition-metal complex probes *via* phosphorescence quenching and lifetime mapping is ideal for measuring dynamic O_2 concentrations, as the luminescence changes are reversible (the excited state can be generated over and over again for repeat measurements), conducted in real-time, are non-invasive, and the probes have the long-term photostability required for large numbers of repeat measurements. However, to truly understand the workings of mitochondria, the ability to perform quantitative [O_2] measurements needs to be combined with high-resolution spatial imaging. Mitochondria exist as a complex network of tubules with elaborate inner folded membranes that are intricately interconnected with other cellular organelles.[1,21] Therefore, comparisons across imaging techniques that can break the diffraction limit, as sub-cellular structures are small in comparison to the resolution limit available using visible light (*ca*. 200 nm), are necessary to help interpret quantitative measurements.

A number of emission-based super-resolution techniques have already proved successful in imaging mitochondria beyond the diffraction limit. For example, *d*STORM (*direct* stochastic optical reconstruction microscopy) has been used to extract detailed information about inner membrane protein locality and density in mitochondria,[22] and STED (stimulated emission depletion microscopy) has been used to investigate clustering of outer membrane proteins[23] and to determine the co-localisation of anion channel hVDAC and cytosolic protein hexokinase-I.[24]

Despite the advances in super-resolution imaging over recent years, there are still very few examples of imaging beyond the diffraction limit[25] using transition metal based dyes or probes.[26] Combining the power of such imaging techniques with an O_2 sensor would be a significant step forward.

In this report, we present the use of two mononuclear Ir(III) complexes as some of the first examples of organelle-specific probes that are compatible with both super-resolution and Transmission Electron Microscopy (TEM) at the same concentration (50 μM). The excellent photostability and low toxicity exhibited by our complexes has enabled them to be utilised in detailed co-staining studies using steady-state confocal and 3D-SIM microscopy, and their long lived triplet emissive states permit O_2 detection *in-vitro,* using two-photon PLIM and lifetime mapping.

Results and Discussion

Synthesis. Octahedral complexes of Ir(III) with a basic ligand framework comprised of two cyclometalating phenyl-pyridine (C^N), ligands and an aromatic N^N ligand such as 2,2-bipyridine, have become some of the most highly studied phosphorescent metal complexes due to the combination of ease of synthesis, ability to tune properties over a wide range with ligand substituents, and outstanding emission lifetime and quantum yield characteristics. As such, complexes of the general formula $[Ir(C^N)_2(N^N)]^+ X^-$ have demonstrated promise across a range of applications based on their photophysical properties such as live cell imaging,[27-30] OLEDs,[31] dye sensitised solar cells[32,33] and sensors;[34,35] in addition the presence of a third-row metal ion would makes such complexes useful as TEM stains.

Here we report two mono-nuclear Ir(III) complexes, Ir-L^{pytz} and Ir-L^{tol} (Scheme 1), which feature this $[Ir(C^N)_2(N^N)]^+$ motif in which the N^N unit is a pyridyl-triazole chelate.[36] The two complexes have the same ligand core but differ in the nature of the group pendant from the C^5 position of the triazole ring ligand, which is a pyridyl group in L^{pytz} and a tolyl group L^{tol} as shown in Scheme 1. The phenyl-pyridine (C^N) co-ligand in both complexes is substituted with a polyethylene glycol chain to enhance water solubility. We found that preparing the C^N ligand with a pendant formyl group, incorporating this into the mononuclear Ir(III) complexes, and then reducing the aldehyde to an alcohol and PEG-ylation as the final steps, provided the highest yielding route to the target complexes.

Steady-state and time resolved photophysical studies. UV-Vis absorption and emission parameters (wavelength, lifetime and quantum yield) for both complexes **Ir-L^{pytz}** and **Ir-L^{tol}** are presented in Table 1. Both complexes exhibited moderate solubility in water at low concentrations. However, to ensure that complex precipitation was not affecting photophysical characterisation, working concentrations of aqueous solutions (typically 50 μM) were prepared by dilution of a 20 mM DMSO stock solution of each complex, to give final solutions containing < 0.5% DMSO. Similar dilutions were used with cell media for cell imaging investigations.

Both complexes displayed broad transitions in the UV-Vis (> 350 nm) region consistent with the expected spin-allowed and spin-forbidden transitions which are generally assigned to a combination of MLCT [$d\pi(Ir) \rightarrow \pi(N^N$ and $C^N)$] and intra-ligand (C^N-based) excited states. The more intense absorption bands below 300 nm are assigned to ligand-centred π-π^* transitions. At neutral pH, both complexes exhibit a structured emission profile typical of an excited state containing some intra-ligand character, with moderate quantum yields of 5 – 9% (Table 1).

Emission lifetimes in air-equilibrated water were best fit to a single exponential decay and were found to be similar for both complexes at neutral pH at > 500 ns. However, upon switching to organic solvents (MeCN, toluene or CH_2Cl_2), the emission quantum yield decreased significantly and the emission lifetime also substantially decreased. In all three cases two luminescence decay components could be detected, with a dominant short-lived component having $\tau < 100$ ns and a minor long-lived component having a lifetime in the 100 – 300 ns range: fitting of the time-resolved emission profile to a double exponential decay was necessary in order to obtain acceptable residual fitting and chi-squared values.

The significant differences in emission quantum yields and lifetimes between water and non-polar organic solvents might, in part, arise from the known conformational flexibility of the peripheral PEG chains between different solvent systems,[37,38] which has been shown by Lo and co-workers to result in solvent-dependent luminescence behaviour in Ir(III) complexes with long pendant PEG units.[39] However the PEG chains in the new complexes that we report in this paper are rather short. An additional factor responsible for the solvent-dependence could be the externally-directed basic N^4 atom at position 4 of the triazole ring which is likely to participate in hydrogen-bonding interactions with solvent molecules,[40] accounting for the difference between the luminescence behaviour in water on the one hand, and MeCN / CH_2Cl_2 / toluene on the other; we note that other types of complex with externally-directed lone pairs from cyanide ligands are well known to display strong solvent dependence of their photophysical properties due to changes in hydrogen-bonding with the solvent.[41]

pH sensitivity of Ir-L^{pytz}. The emission properties of **Ir-L^{pytz}** were monitored over the pH range 1 – 12 to assess the effect of protonation on the pendant pyridyl unit. Under basic conditions (pH > 8) the emission of **Ir-L^{pytz}** remained similar to that observed under neutral

conditions (see Fig. 1). However, upon lowering the pH the emission intensity was quenched significantly. The largest decrease in emission intensity (63%) was observed between pH 7 and pH 4, as shown by Fig. S9, which is the pH range where protonation of the pendant pyridyl group should be expected. The partial quenching of emission intensity was also accompanied by a reduction in emission lifetime from 520 ns to 350 ns, and is believed to be due to photoinduced electron transfer between the metal centre and the protonated pyridinium unit.[45,46] Although **Ir-L^{pytz}** does show a clear response across physiological pH, it is often more desirable for a pH probe to exhibit an increase in intensity (or a shift in λ_{max}) upon protonation. No change in emission intensity was expected or observed for **Ir-L^{tol}** in the same pH window as this complex lacks a pendant pyridyl unit.

Confocal microscopy and co-localisation studies. Both complexes were screened for cellular uptake and toxicity using live HeLa cells. Time-dose experiments across the 10-75 μM concentration range at 15 min, 1 h, 4 h, 18 h and 24 h were carried out to establish optimal staining conditions. **Ir-L^{tol}** was observed to be slightly less soluble in aqueous media than **Ir-L^{pytz}**, occasionally leading to small amounts of precipitated complex in the incubation media. Short incubation times of ≤1 h did not provide a suitable level of cellular emission for confocal imaging, implying that these complexes enter the cell *via* an energy dependent pathway.[47] Extending the incubation period to 4 h led to clear cellular emission for both complexes, which could be observed using 405 nm excitation. As expected, emission intensity increased with incubation time, however as images obtained after 4 h were of good quality, this was selected as the optimal incubation time for further studies. The optimal loading concentration for a 4 h incubation period was 50 μM, which provided a good level of emission intensity and contrast,

without overloading the cells with complex or requiring high gain settings. A typical confocal image showing the staining pattern of both complexes can be seen in Fig. S11.

Cell morphology and number remained consistent across all incubations with respect to control cells containing no Ir complex, including those at much longer times with high doses (>18 h, 75 μM). This suggests that both **Ir-L^{pytz}** and **Ir-L^{tol}** exhibit insignificant cytotoxic effects on living cells. This observation was confirmed by MTT toxicity assays, which measures cell metabolic activity. Fig. S10 shows that there was no significant change in cell metabolic activity in comparison to control cells, after treatment with either complex for 4 h at 10 – 75 μM, confirming that cells remained viable after incubation with either **Ir-L^{pytz}** or **Ir-L^{tol}**.

Once internalised by the cells under optimal conditions (50 μM, 4 h) both **Ir-L^{pytz}** and **Ir-L^{tol}** exhibit very similar staining patterns (Fig. 2, left), appearing as a structured network within the cell cytoplasm. No nuclear staining was observed implying that neither complex can cross the nuclear membrane, a feature commonly observed for these types of cyclometalated Ir(III) complex.[48] To confirm cellular localisation of the complexes in HeLa cells, co-staining studies were carried out with MitoTracker® Orange and CellLight® ER-RFP. Mitochondria and endoplasmic reticulum organelles both resemble a network of membranes when stained and imaged under confocal microscopy. Therefore, these co-stains were considered the most appropriate starting point to investigate localisation of **Ir-L^{pytz}** and **Ir-L^{tol}**. The degree of co-localisation was evaluated by quantitative (Manders and Pearson's coefficients)[49] and qualitative (image overlay) methods. Co-occurrence and co-localisation coefficients are given for each co-stain in Table 2.

Co-localisation experiments with MitoTracker ® Orange. A small degree of off-target nucleoli staining was observed when using MitoTracker ® Orange (Fig. 2, middle). Despite this,

the Pearson's coefficients for **Ir-L^{pytz}** and **Ir-L^{tol}** with MitoTracker® Orange were 0.72 and 0.73, suggesting there is a large degree of co-localisation between the probes and the commercial mitochondrial stain. This is supported by the high degree of co-occurrence demonstrated by the excellent Manders coefficents of 0.91 and 0.96, respectively, as well as the qualitative data in Fig. 2 (where white pixels depict co-occurrence between green and red channels). The co-localisation and co-occurrence data strongly suggest that **Ir-L^{pytz}** and **Ir-L^{tol}** accumulate in the mitochondria of living cells. It is also likely that the true amount of co-localisation is slightly higher than the Pearsons coefficient implies, as this measurement also takes into account the off-target emission observed for MitoTracker® Orange. Manders values were calculated using emission from the green channel as a starting point *('if there is a green, is there a red?')*, therefore these values are not skewed by off target MitoTracker® staining.

To ensure that there was no cross-talk between MitoTracker® Orange and the probe complexes, and that quantitative measurements were robust, control experiments were also carried out. HeLa cells treated solely with MitoTracker® Orange were imaged using 405 and 561 nm excitation and emission filters 525/50 nm (green) and >590 nm (red). MitoTracker® should ideally only exhibit emission in the red channel under 561 nm excitation. However, Fig. S13 also shows that a small amount of MitoTracker® emission is observed in the red channel under 405 nm excitation. As all emission from MitoTracker® Orange is confined to the red channel, it does not interfere with iridium-based emission collected from dual-stained samples (Ir-based emission is collected from the green channel only under 405 nm excitation, and neither Ir-L^{pytz} or Ir-L^{tol} are emissive under 561 nm excitation). This confirms that there is no-cross talk between Ir-based and MitoTracker® emission, giving a high degree of confidence in the co-

localisation analysis and the conclusion that Ir-L^{pytz} and Ir-L^{tol} accumulate at the mitochondria of living cells.

The fact that both complexes exhibited a very similar staining pattern was initially surprising, as the pH sensitive pyridyl moiety on Ir-L^{pytz} might be expected to have some influence on directing cellular localisation. As Ir-L^{pytz} becomes protonated in the pH 4-6 region, it was expected to localise in the lysosomes where the local acidic pH would protonate and subsequently trap the complex.[51,52] The staining observed (Fig. 2) is clearly not indicative of lysosomal staining, which typically appears as bright punctate pattern throughout the cell cytoplasm (as indicated by Fig. S14), suggesting that the pendant pyridyl unit is not actually directing the cellular localisation in this way. It is possible that Ir-L^{pytz} accumulates in the lysosomes in addition to the mitochondria, however the extent of this is difficult to ascertain *via* steady-state confocal imaging, especially as the emission intensity of Ir-L^{pytz} is partly quenched upon protonation.

Super-resolution imaging: 3D-SIM. Very few transition metal complexes have been used in conjunction with emission imaging that goes beyond the diffraction limit,[25,26] though their excellent photostability makes them good candidates. In order to generate a good quality reconstructed SIM image, the emissive molecule / probe must demonstrate a high emission intensity and specific organelle binding. Although quantum yield values for **Ir-L^{pytz}** and **Ir-L^{tol}** are relatively modest, they performed well in confocal imaging in terms of emission intensity and stability under prolonged irradiation. They also exhibit specific organelle staining, as demonstrated by the colocalisation studies with MitoTracker® Orange. Therefore, **Ir-L^{pytz}** and **Ir-L^{tol}** were investigated as 3D-SIM probes.

HeLa cells incubated with either **Ir-L^{pytz}** or **Ir-L^{tol}** (50 μM, 4 h) were washed and fixed, before mounting with prolong™ gold antifade mountant for 3D-SIM. The emission intensity from both **Ir-L^{pytz}** and **Ir-L^{tol}** under 405 nm irradiation was sufficient for image reconstruction. However, the poorer solubility observed for **Ir-L^{tol}** was found to be problematic. Unlike confocal microscopy, where only one focal plane is required to record an image, 3D-SIM requires an array of images taken across the Z plane. Hence, out-of-focus light from a small amount of complex precipitate that would be rejected in a confocal microscopy measurement becomes a significant problem for image reconstruction (see Fig. S16). Although some clear mitochondrial staining can be observed for **Ir-L^{tol}** in Fig. S16, this solubility issue led us to concentrate on **Ir-L^{pytz}** for further 3D-SIM studies.

HeLa cells stained with **Ir-L^{pytz}** clearly show that the complex is staining a network of tubular membranes across the cell cytoplasm. Co-stained HeLa cells, incubated with **Ir-L^{pytz}** followed by MitoTracker® Orange (100 nM, 20 mins) show that the staining patterns of **Ir-L^{pytz}** and MitoTracker® Orange overlap throughout the cell cytoplasm. The additional resolution afforded by 3D-SIM reveals that (i) **Ir-L^{pytz}** also accumulates at the nuclear membrane (Fig. S17, blue arrows); and (ii) some regions of the cell cytoplasm exhibit emission from the green channel only. These regions (see Fig. S17) could be due to additional lysosomal staining of **Ir-L^{pytz}**, however, due to extremely rapid photobleaching of the commercial LysoTracker® Red it was not possible to obtain high resolution 3D-SIM, co-stained images. It is also a possibility that these regions of green emission are a product of imaging processing, as the modulation contrast-to-noise ratio is only moderate for **Ir-L^{pytz}** (6-10) in comparison to MitoTracker® Orange (18-24). 3D-SIM image analysis was carried out using SIMcheck;[53] the modulation contrast-to-noise ratio (MCNR) is a measure of how many photons are being detected and is a key metric for the

strength of a SIM reconstruction. Values of < 3 are considered to be inadequate for reconstruction, 6-11 are rated as adequate and 12-24 are good-to-excellent.

It is clear that **Ir-L^{pytz}** and MitoTracker® are very well correlated within the cell cytoplasm. Line profiles (Fig. 3, C & D) show that the distribution of MitoTracker® emission is slightly narrower with respect to **Ir-L^{pytz}** per mitochondrial cross section; and that the profile of **Ir-L^{pytz}** has two maxima per cross section whereas MitoTracker® only has one. This data suggests that **Ir-L^{pytz}** tends to stain the mitochondrial membrane, whereas MitoTracker® accumulates within the mitochondria.

Line profiles taken from HeLa cells stained with **Ir-L^{pytz}** only exhibit the same distribution of emission intensity (Fig. S15), with two maxima per mitochondrion arising from staining at the mitochondrial membranes (edges) and a slight reduction in emission intensity at the centre. The fact that the edge-to-centre ratio of **Ir-L^{pytz}** emission intensity is not reduced in the presence of MitoTracker® Orange also suggests that these two species are not competing for exactly the same binding site at the mitochondria.

The photostability of **Ir-L^{pytz}** was also assessed against MitoTracker® Orange, using SIMcheck (ImageJ plug-in), as this is a key factor in producing high-quality SIM reconstruction. After acquisition of 700 raw images, **Ir-L^{pytz}** was found to exhibit a small intensity decay of 2.6%, whereas MitoTracker® Orange had decayed by 32.1%. This clearly demonstrates that **Ir-L^{pytz}** has much greater photostability than the commercial MitoTracker® dye (see Fig. S18). Intensity fluctuations observed between and within angles appear to be a systematic issue with metal complexes, based on our recent investigations of several transition metal complex probes for 3D-SIM.[54] We currently tentatively attribute these fluctuations to intrinsic properties of

luminescent metal complexes, for example their long emission lifetimes in comparison to commercial organic fluorophores.

TEM imaging studies. There is currently only a handful of studies in which transition metal complexes have demonstrated contrast enhancement in TEM,[55-58] despite the excellent ability of such complexes to scatter electrons. Of these, very few are mono-nuclear species.[58-59] With the recent developments and growth in correlative microscopy[60-62] it would be advantageous to design a single probe that is compatible with both emission and electron microscopy techniques. As Ir-based complexes combine excellent photophysical properties with the high electron density needed for use as TEM stains, and **Ir-L^{pytz}** and **Ir-L^{tol}** demonstrate good specificity for cellular mitochondria, these complexes were further investigated in TEM with and without the use of typical contrast agents.

Live HeLa cells treated with **Ir-L^{pytz}** and **Ir-L^{tol}** (50 μM, 4 hours) were fixed using glutaraldehyde (3%) in PBS, dehydrated, and embedded in araldite resin before being sectioned and imaged using TEM. When stained with one of the Ir complexes only (Fig. S19), obvious contrast enhancement was observed throughout the cytoplasm in comparison to untreated control cells. A number of tubular structures that make up a larger network appeared to show enhanced contrast when compared to the surrounding cytoplasm. These organelles were expected to be the mitochondria based on the emission microscopy studies. However, very little cytoplasmic structure is visible in untreated cells under TEM, making it difficult to confirm the nature of the enhancement brought about by the addition of **Ir-L^{pytz}** or **Ir-L^{tol}**. Therefore, cells containing both an Ir complex *and* typical contrast agents, osmium tetroxide (OsO_4), lead citrate (LC) and uranyl acetate (UA), were investigated.

Upon addition of OsO_4, LC and UA to control cells (containing no Ir complex), organelle membranes and mitochondrial cristae become visible (Fig. 4, bottom-centre), revealing the shape and distribution of the mitochondria thought the cell cytoplasm. Where cells have additionally been pre-treated with either **Ir-L^{pytz}** or **Ir-L^{tol}** (Fig. 4, left & right) the mitochondria appear as dark (filled) vesicles with sharp, distinct edges, while the rest of the cells appears similar to the control sample. Thus, accumulation of the Ir complex at the mitochondria before fixation enhances the contrast of this organelle drastically, so much so that that the mitochondrial cristae become obscured in some cases.

Rather than just relying on qualitative interpretation of TEM data, we attempted to quantify the amount of contrast enhancement brought about by the addition of **Ir-L^{pytz}** and **Ir-L^{tol}**, using equation 1 to calculate the relative contrast (RC). To implement this, an internal reference (area containing no cells) was necessary in each TEM image under investigation. The internal reference is an area of resin where the intensity of electrons passing through the sample is assumed to be the same as that entering the sample (E_{in}), as there is no cellular material to scatter the electron beam. E_{in} was therefore calculated as an average from a large area of resin (~ 3.72 μm in diameter) typically comprising around 8.0 x 10^4 pixels (Fig. 5). Variation in E_{in} across a sample is generally limited to a few percent, as the thickness of a 85 nm section only varies by a maximum of +/- 2 nm, giving an overall worst-case error of *ca.* 5%.[63] E_{in} values are not transferable between images, as sample thickness and image acquisition parameters affect intensity histograms extracted using imageJ.

$$RC = 1 - (E_{out} / E_{in}) \qquad \text{(Eq. 1)}$$

RC is the relative contrast between a region of interest (containing cellular material) and the internal reference (resin only). E_{out} is calculated by the intensity of electrons per pixel leaving the sample after passing though the region of interest. (Note that RC is measured on a scale of 0 to 1: a value of 0 would mean that none of the electrons are scattered by the sample, with respect to the resin, therefore E_{out} and E_{in} would be the same. A value of 1 would mean that all of the electrons hitting the sample were scatteredand E_{out} would therefore be 0. The greater the electron density of the nuclei present, the greater the scattering will be).

The primary region of interest in this study is the mitochondria. However, qualitative analysis of TEM images in the absence of an Ir complex showed that addition of OsO_4, LC and UA generally increased the contrast of the cell cytoplasm, in comparison to completely untreated cells. Therefore, it was important to calculate and compare the RC values for a region of the cytoplasm without mitochondria present, as well as the mitochondria themselves.

Fig. 5 depicts the images that were used for this analysis. Three different mitochondria were selected (green boxes) and their mean signal intensities averaged to give organelle E_{out} values. Areas of cytoplasm (blue boxes) containing no obvious membranes or organelles were selected and histograms of these areas (extracted using imageJ) were calculated to obtain cytoplasm-only E_{out} values for each cell. For cells that had not been pre-treated with **Ir-L^{pytz}** or **Ir-L^{tol}** the difference in relative contrast between the cytoplasm and the mitochondria was 3.4%. This difference is attributed to the large volume of mitochondrial membrane which make up the cristae. The differences in RC between cytoplasm and mitochondria in cells treated with **Ir-L^{pytz}** and **Ir-L^{tol}** are significantly higher at 6.3% and 10%, respectively. Interestingly, **Ir-L^{tol}** appears to provide marginally better contrast enhancement than **Ir-L^{pytz}**, suggesting that although the

complex does display solubility problems, it may actually target the mitochondria more efficiently than **Ir-L^{pytz}**.

One of the most interesting observations arising from this TEM work is the fact that these complexes provide excellent contrast under the same loading concentration (50 μM) as used for emission microscopy. Previously, transition metal complexes that have been successfully applied to TEM imaging have required loading concentrations of ≥100 μM[59] to achieve sufficient image contrast, which is typically much higher than usually required for luminescence imaging.

Oxygen sensing using two-photon PLIM. Time-resolved imaging methods, such as Phosphorescence Lifetime Imaging Microscopy (PLIM), provide the ability to acquire additional detail about the cellular microenvironment[9,12,17,64-66] in a real-time and relatively non-invasive way. The long-lived triplet excited states of **Ir-L^{pytz}** and **Ir-L^{tol}**, combined with their specific mitochondrial localisation, make them excellent candidates for time resolved *in-vitro* studies. The microenvironment at the mitochondria, in particular the local concentration of O_2, can be investigated *via* Stern-Volmer quenching of the triplet excited state of the Ir-based probe complex. Some progress has been made in this area recently,[12] however the use of super-resolution imaging and TEM to identify cellular localisation with such certainty, coupled with quantitative and real-time O_2 measurements, is a relatively unexplored partnership of substantial current interest.

In order to understand the emission response of our iridium complexes to a change in O_2 concentration, PLIM investigations were initially carried out in both water and cell media (DMEM, see ESI for full details) solutions. As the lifetime and quantum yield of **Ir-L^{pytz}** and **Ir-L^{tol}** were similar to one another in aqueous solvents, **Ir-L^{pytz}** was selected as the lead compound

for these oxygen sensing studies due to its better solubility. Solution PLIM measurements were carried out using the same instrument set-up used for *in-vitro* measurements, with solutions placed in a MatTek glass-bottomed culture dishes. This was to ensure that solution data could be closely compared with *in-vitro* studies. Emission decays were best fit to a single exponential decay model, using Becker & Hickl SPCImage (version 5).

Stern-Volmer plots (Fig. 6) show the emission lifetime response of **Ir-L^{pytz}** in water and cell media under varying concentrations of O_2. Gas mixtures of N_2 and O_2 were applied by a positive stream of controlled gas delivered to a sealed chamber. Samples were equilibrated for 20 minutes on the microscope stage before data collection. Stern-Volmer quenching constants in water and DMEM media were concluded to be $K_{sv} = 2.08\text{x}10^{-3}$ μM^{-1} and $K_{sv} = 3.02\text{x}10^{-3}$ μM^{-1}, respectively. Although these quenching constants are not as large as some large porphyrin-based O_2 sensors,[8] they are similar to those published by Keyes and co-workers, who reported on the mitochondrial response to Antimycin A (a mitochondrial uncoupler which changes the local oxygen concentration and affects ATP production),[67,68] using a Ru(II) complex.[12]

The slight difference between the quenching constants of **Ir-L^{pytz}** in water and media solutions stems from the different emission lifetimes in the absence of O_2. Lifetimes measured at elevated levels of oxygen (345 to 1387 μM) were very similar across both solvent systems, i.e. the values were within experimental error of one another. However, at 0 μM of O_2, when the incoming stream of gas is 100% N_2, the emission lifetime for **Ir-L^{pytz}** is longer in cell media (1100 ns) than in water (750 ns). This is attributed to the high proportion of protein molecules present in cell media to which **Ir-L^{pytz}** can bind, protecting it from quenching effects of the bulk solution. This rationale is supported by previous studies that also demonstrate how binding to a protein can lead to an increase in emission intensity in transition metal complexes.[69-71] This

protection offered by protein binding may only be noticeable in the absence of O_2, as lifetime shortening by collisional quenching with O_2 masks the subtle solvent effects as $[O_2]$ increases.

Using the same incubation conditions as established for the imaging studies, HeLa cells were loaded with **Ir-L^{pytz}** (50 μM, 4h), washed with PBS, and covered with fresh media before imaging the cells by PLIM without fixation. Emission decay profiles, per-pixel, were best fit to a double exponential decay model. The major component (τ_1, contributing 75-80% of total emission intensity) was used to plot rainbow colour maps and distribution histograms. Fig. 7 depicts the progression of emission lifetime *in vitro* upon altering the O_2 concentration surrounding the cell. Shorter lifetimes are represented by warm colours (red-orange) and longer lifetimes are represented by cool colours (blue). The histogram shows the lifetime distribution of the major lifetime component across the entire cell located in the centre of the field-of-view. Fig. 7 clearly demonstrates that **Ir-L^{pytz}** retains sensitivity in detecting changes to local concentrations of O_2, even when bound within cellular mitochondria.

Emission lifetimes in live cells appear to be longer than those recorded in cell media under the same externally applied O_2 concentration. We attribute this difference to the fact that **Ir-L^{pytz}** is closely associated with the mitochondria inside the cell. Elongated lifetimes with respect to cell media could be due to the nature of the binding site at the mitochondria, or local O_2 concentration being lower due to its consumption in cell respiration and production of ATP, or a combination of both. In addition to whole cell field-of-view analysis presented in Fig. 7, more specific mitochondrial regions of interest (ROI) were also investigated. Mitochondrial lifetimes were compared across two sample sets: Sample A comprised several different cultured cell samples, all incubated with the same concentration of **Ir-L^{pytz}**. Sample B was a single cell FOV. Each sample set was investigated across the same set of O_2 concentrations. This was to

establish reproducibility and to ensure that prolonged irradiation of a single FOV was not having adverse effects on the emission properties of the internalized **Ir-L^{pytz}**.

Fig. 8, left, shows the superimposed data from both sample sets. Average τ_1 values were calculated from 10 mitochondrial ROI's across a FOV, where errors bars depict the standard deviation about the average. Orange data points represent sample set A, in which a different cell FOV was analysed at each O_2 concentration, whereas blue data points represent sample set B, where the same individual cell was irradiated across all O_2 concentrations. This data shows excellent correlation between the two sample sets indicating that either method could be used to probe the emission lifetime of the probe in the cell. Fig. 8 also shows that repeated atmosphere equilibration, and prolonged photo-excitation of a single sample dose, provided robust and repeatable emission lifetime data. The emission spectrum (Fig. 8, right) taken from a live cell after PLIM imaging also implies that the emissive complex remains intact under prolonged two-photon irradiation.

Conclusions

These [Ir(N^C)$_2$(N^N)] complexes are amongst the first examples of transition metal probes that demonstrate compatibility with both super-resolution emission imaging (3D-SIM) and transmission electron microscopy (TEM) imaging.[72] The fact that **Ir-L^{pytz}** and **Ir-L^{tol}** are compatible with both techniques at the same moderate loading concentration (50 μM), is a significant improvement compared to other transition metal TEM probes. This also opens the possibility for these Ir(III) complexes to be applied to the emerging techniques of Correlative Light and Electron Microscopy (CLEM).[62] CLEM offers the potential to truly compare imaging data from the precisely the same field of view, within the same cell sample, thereby enabling the

dynamics of complex processes to be investigated and rare events to be explored at a cell ultrastructure level. The combination of CLEM plus quantitative O_2 sensing would be potentially very powerful for extracting information concerning cellular processes.

The specific mitochondrial localization observed for **Ir-L^{pytz}** and **Ir-L^{tol}** was corroborated by detailed co-localisation studies using MitoTracker® Orange, and TEM microscopy with the traditional contrast agents OsO_4, lead citrate and uranyl acetate. The fact that contrast enhancement was observed *only* at the mitochondria in the presence of an Ir complex, suggests that the additional 'green' emission, which did not match MitoTracker® Orange in the 3D-SIM images, is most likely due to image processing rather than lysosomal staining. To improve image reconstruction, the complex would need to exhibit a higher MCNR, which can only be achieved by increasing the quantum yield. Although the MCNR was modest for **Ir-L^{pytz}**, it was sufficient to clearly observe the interconnecting tubular structure of the mitochondria. In addition, the superior performance of **Ir-L^{pytz}** in terms of photostability in 3D-SIM with respect to commercial stains is also worth noting.

The O_2 sensing ability of **Ir-L^{pytz}** was observed to be moderate in aqueous solution, yet this level of sensitivity was not reproducible *in vitro*. However, the fact that **Ir-L^{pytz}** retained some sensitivity towards external changes in O_2 concentrations whilst bound at the mitochondria, is promising.

Overall, the specific organelle staining coupled with excellent photostability make these Ir(III) complexes very promising starting points from which to develop CLEM probes. Moreover, their promising ability to detect O_2 changes whilst bound at the mitochondria make them excellent candidates to develop a organelle specific multi-modal imaging probe.

Experimental Section

See ESI for full synthesis and characterisation details of all compounds listed in Scheme 1 and corresponding NMR spectra. General cell culture and staining protocols can also be found in the EDI, along with oxygen sensing parameters and PLIM data analysis.

3D SIM imaging. For 3D SIM, cells were seeded in 6-well plates on high precision coverslips and grown to ~60% confluency. After the growth media was removed, the cells were washed with PBS (1 x 1 mL) and then treated with 50 μM **Ir-L^{pytz}** or **Ir-L^{tol}** in full DMEM (<1% DMSO) at 37 °C for 2 h. The media was then removed, the cells washed with PBS (1 x 1 mL) and then fixed using 4% paraformaldehyde in PBS for 10 minutes. Finally, the cover slips were dipped in deionised water to remove any salts on the cover slip, mounted on microscope slides using Slowfade® gold antifade reagent and then imaged. All 3D SIM imaging was performed on a GE Deltavision OMX blaze in structured illumination mode using fixed HeLa cells. Ir complexes were excited using 405 nm with a filter set of 528/20 nm. MitoTracker® Orange was imaged using 561 nm excitation with a filter set of 600/37 nm, imaging was performed sequentially and channels were corrected using the provided software tool. All SIM reconstructions were performed on Softworx version 6.5.2 (GE healthcare) using OTFs optimised for the specific wavelength and oil used. Images were run through the Image J plugin SIM check. Further image analysis was performed on Imaris 7.1 (Bitplane AG, Switzerland).

TEM imaging. Cells were cultured in T-25 flasks to 90% confluency. After the growth media was removed, the cells were washed with PBS and the stained with 50 μM Ir-L^{pytz} or Ir-L^{tol} in full DMEM(<2% DMSO) at 37 °C for 4 h, washed with PBS (5 mL) and fixed using glutaraldehyde (2.5% in PBS) overnight at 4 °C. Cells were then dehydrated using ethanol, embedded in Araldite resin and sectioned by microtome before imaging by TEM. All TEM was

carried out using a FEI Tecnai 120Kv G2 Biotwin TEM operating at 80 kV equipped with an Orius SC100 bottom-mounted camera using Gatan Digital Micrograph software.

Acknowledgements

We thank the University of Sheffield for PhD studentships (JRS, AJC, LKM and BJC) and access to the Wolfson Light Microscopy Facility. The Central Laser Facility at the Rutherford Appleton Laboratory received funding from the European Union's Horizon 2020 research and innovation programme under grant agreement no. 654148 (Laserlab-Europe).

Supporting Information. The following file is available free of charge as a PDF file: Full experimental details including synthesis and characterisation details of new complexes; details of cell culture and imaging methods and MTT toxicity data; additional steady-state confocal microscopy, 3D-SIM and TEM images; PLIM analysis of HeLa cells under atmosphoeric conditions; additional references (PDF).

Author Contributions. The manuscript was written through contributions of all authors. All authors have given approval to the final version of the manuscript.

References

(1) Nunnari, J.; Suomalainen, A. Mitochondria: in sickness and in health. *Cell* **2012**, *148*, 1145-1159.

(2) Yotter, R. A.; Wilson, D. M. Sensor technologies for monitoring metabolic activity in single cells-part II: nonoptical methods and applications. *IEEE Sens. J.* **2004**, *4*, 412-429.

(3) Dewhirst, M. W.; Secomb, T. W.; Ong, E. T.; Hsu, R.; Gross, J. F. Determination of Local Oxygen Consumption Rates in Tumors. *Cancer Res.* **1994**, *54*, 3333-3336.

(4) Arteel, G. E.; Thurman, R. G.; Yates, J. M.; Raleigh, J. A. Evidence that hypoxia markers detect oxygen gradients in liver: pimonidazole and retrograde perfusion of rat liver. *Brit. J. Cancer* **1995**, *72*, 889-895.

(5) Diepart, C.; Verrax, J.; Calderon, P. B.; Feron, O.; Jordan, B. F.; Gallez, B. Comparison of methods for measuring oxygen consumption in tumor cells in vitro. *Anal. Biochem.* **2010**, *396*, 250-256.

(6) Dmitriev, R. I.; Zhdanov, A. V.; Ponomarev, G. V.; Yashunski, D. V.; Papkovsky, D. B. Intracellular oxygen-sensitive phosphorescent probes based on cell-penetrating peptides. *Anal. Biochem.* **2010**, *398*, 24-33.

(7) Fercher, A.; Borisov, S. M.; Zhdanov, A. V.; Klimant, I.; Papkovsky, D. B. Intracellular O_2 Sensing Probe Based on Cell-Penetrating Phosphorescent Nanoparticles. *ACS Nano* **2011**, *5*, 5499-5508.

(8) Papkovsky, D.; Zhdanov, A. V.; Fercher, A.; Dmitriev, R. I.; Hynes, J. Phosphorescent oxygen-sensitive probes (Springer, Basel) **2012**.

(9) Sakadžić, S.; Roussakis, E.; Yaseen, M. A.; Mandeville, E. T.; Srinivasan, V. J.; Arai, K.; Ruvinskaya, S.; Devor, A.; Lo, E. H.; Vinogradov, S. A.; Boas, D. A. Two-photon high-resolution measurement of partial pressure of oxygen in cerebral vasculature and tissue. *Nat. Meth.* **2010**, *7*, 755-759.

(10) Kazmi, S. M. S.; Salvaggio, A. J.; Estrada, A. D.; Hemati, M. A.; Shaydyuk, N. K.; Roussakis, E.; Jones, T. A.; Vinogradov, S. A.; Dunn, A. K. Three-dimensional mapping of oxygen tension in cortical arterioles before and after occlusion. *Biomed. Opt. Express* **2013**, *4*, 1061-1073.

(11) Khan, A. A.; Fullerton-Shirey, S. K.; Howard, S. S. Easily prepared ruthenium-complex nanomicelle probes for two-photon quantitative imaging of oxygen in aqueous media. *RSC Adv.* **2015**, *5*, 291-300.

(12) Martin, A.; Byrne, A.; Burke, C. S.; Forster, R. J.; Keyes, T. E. Peptide-Bridged Dinuclear Ru(II) Complex for Mitochondrial Targeted Monitoring of Dynamic Changes to Oxygen Concentration and ROS Generation in Live Mammalian Cells. *J. Am. Chem. Soc.* **2014**, *136*, 15300-15309.

(13) Lv, W.; Yang, T.; Yu, Q.; Zhao, Q.; Zhang, K. Y.; Liang, H.; Liu, S.; Li, F.; Huang, W. A Phosphorescent Iridium(III) Complex-Modified Nanoprobe for Hypoxia Bioimaging via Time-Resolved Luminescence Microscopy. *Adv. Sci.* **2015**, *2*, 1500107.

(14) Baggaley, E.; Weinstein, J.; Williams, J. A. G. Time-Resolved Emission Imaging Microscopy Using Phosphorescent Metal Complexes: Taking FLIM and PLIM to New Lengths. *Struct. Bonding (Springer, Berlin)* **2014**, *165,* 205–256.

(15) Yoshihara, T.; Hirakawa, Y.; Hosaka, M.; Nangaku, M.; Tobita, S. Oxygen imaging of living cells and tissues using luminescent molecular probes. *J. Photochem. Photobiol. C: Photochem. Rev.* **2017**, *30*, 71-95.

(16) Dmitriev, R. I.; Papkovsky, D. B. Intracellular probes for imaging oxygen concentration: how good are they? *Methods Appl. Fluoresc.* **2015**, *3*, 034001.

(17) Dmitriev, R. I.; Kondrashina, A. V.; Koren, K.; Klimant, I.; Zhdanov, A. V.; Pakan, J. M. P.; McDermott, K. W.; Papkovsky, D. B. Small molecule phosphorescent probes for O_2 imaging in 3D tissue models. *Biomat. Sci.* **2014**, *2*, 853-866.

(18) Lecoq, J.; Parpaleix, A.; Roussakis, E.; Ducros, M.; Houssen, Y. G.; Vinogradov, S. A.; Charpak, S. Simultaneous two-photon imaging of oxygen and blood flow in deep cerebral vessels. *Nat. Med.* **2011**, *17*, 893-898.

(19) Yu, Q.; Huang, T.; Li, Y.; Wei, H.; Liu, S.; Huang, W.; Du, J.; Zhao, Q. Rational design of a luminescent nanoprobe for hypoxia imaging *in vivo via* ratiometric and photoluminescence lifetime imaging microscopy. *Chem. Commun.* **2017**, *53*, 4144-4147.

(20) Lu, S.; Xu, W.; Zhang, J.; Chen, Y.; Xie, L.; Yao, Q.; Jiang, Y.; Wang, Y.; Chen, X. Facile synthesis of a ratiometric oxygen nanosensor for cellular imaging. *Biosens. Bioelectron.* **2016**, *86*, 176-184.

(21) Jakobs, S.; Wurm, C. A. Super-resolution microscopy of mitochondria. *Curr. Opin. Chem. Biol.* **2014**, *20*, 9-15.

(22) van de Linde, S.; Sauer, M.; Heilemann, M. Subdiffraction-resolution fluorescence imaging of proteins in the mitochondrial inner membrane with photoswitchable fluorophores. *J. Struct. Biol.* **2008**, *164*, 250-254.

(23) Wurm, C. A.; Neumann, D.; Lauterbach, M. A.; Harke, B.; Egner, A.; Hell, S. W.; Jakobs, S. Nanoscale distribution of mitochondrial import receptor Tom20 is adjusted to cellular conditions and exhibits an inner-cellular gradient. *Proc. Nat. Acad. Sci.* **2011**, *108*, 13546-13551.

(24) Neumann, D.; Bückers, J.; Kastrup, L.; Hell, S. W.; Jakobs, S. Two-color STED microscopy reveals different degrees of colocalization between hexokinase-I and the three human VDAC isoforms. *PMC Biophysics* **2010**, *3*, 4.

(25) Huang, B.; Babcock, H.; Zhuang, X. Breaking the Diffraction Barrier: Super-Resolution Imaging of Cells. *Cell* **2010**, *143*, 1047-1058.

(26) Byrne, A.; Burke, C. S.; Keyes, T. E. Precision targeted ruthenium(II) luminophores; highly effective probes for cell imaging by stimulated emission depletion (STED) microscopy. *Chem. Sci.* **2016**, *7*, 6551-6562.

(27) Baggaley, E.; Weinstein, J. A.; Williams, J. A. G. Lighting the way to see inside the live cell with luminescent transition metal complexes. *Coord. Chem. Rev.* **2012**, *256*, 1762-1785.

(28) Thorp-Greenwood, F. L.; Balasingham, R. G.; Coogan, M. P. Organometallic complexes of transition metals in luminescent cell imaging applications. *J. Organomet. Chem.* **2012**, *714*, 12-21.

(29) Coogan, M. P.; Fernandez-Moreira, V. Progress with, and prospects for, metal complexes in cell imaging. *Chem. Commun.* **2014**, *50*, 384-399.

(30) Lo, K. K.-W. Luminescent Rhenium(I) and Iridium(III) Polypyridine Complexes as Biological Probes, Imaging Reagents, and Photocytotoxic Agents. *Acc. Chem. Res.* **2015**, *48*, 2985-2995.

(31) Gildea, L. F.; Williams, J. A. G. Iridium and platinum complexes for OLEDs: Chapter 3 in *Organic Light-Emitting Diodes (OLEDs) – Materials, devices and applications* (Ed. Buckley, A.), Woodhead, UK, **2013**.

(32) Erten-Ela, S.; Ocakoglu, K. Iridium dimer complex for dye sensitized solar cells using electrolyte combinations with different ionic liquids. *Mater. Sci. Semicond. Process.* **2014**, *27*, 532-540.

(33) Baranoff, E.; Kumar, P. Iridium Complexes as Photoactive Center for Light Harvesting and Solar Cell Applications: Chapter 14 in *Iridium(III) in Optoelectronic and Photonics Applications* (Ed. Zysman-Colman, E.), Wiley, Chichester (UK), **2017**

(34) Zhang, K. Y.; Zhang, J.; Liu, Y.; Liu, S.; Zhang, P.; Zhao, Q.; Tang, Y.; Huang, W. Core–shell structured phosphorescent nanoparticles for detection of exogenous and endogenous hypochlorite in live cells via ratiometric imaging and photoluminescence lifetime imaging microscopy. *Chem. Sci.* **2015**, *6*, 301-307.

(35) Liu, S.; Liang, H.; Zhang, K. Y.; Zhao, Q.; Zhou, X.; Xu, W.; Huang, W. A multifunctional phosphorescent iridium(III) complex for specific nucleus staining and hypoxia monitoring. *Chem. Commun.* **2015**, *51*, 7943-7946.

(36) Park, H. J.; Kim, J. N.; Yoo, H.-J.; Wee, K.-R.; Kang, S. O.; Cho, D. W.; Yoon, U. C. Rational Design, Synthesis, and Characterization of Deep Blue Phosphorescent Ir(III) Complexes Containing (4′-Substituted-2′-pyridyl)-1,2,4-triazole Ancillary Ligands. *J. Org. Chem.* **2013**, *78*, 8054-8064.

(37) Li, S. P.-Y.; Lau, C. T.-S.; Louie, M.-W.; Lam, Y.-W.; Cheng, S. H.; Lo, K. K.-W. Mitochondria-targeting cyclometalated iridium(III)–PEG complexes with tunable photodynamic activity. *Biomaterials* **2013**, *34*, 7519-7532.

(38) Pope, S. J. A.; Rice, C. R.; Ward, M. D.; Morales, A. F.; Accorsi, G.; Armaroli, N.; Barigelletti, F. Folding of a poly(oxyethylene) chain as probed by photoinduced energy transfer between Ru- and Os-polypyridine termini. *J. Chem. Soc., Dalton Trans.* **2001**, 2228-2231.

(39) Li, S. P.-Y.; Liu, H.-W.; Zhang, K. Y.; Lo, K. K.-W. Modification of luminescent iridium(III) polypyridine complexes with discrete poly(ethylene glycol) (PEG) pendants: synthesis, emissive behaviour, intracellular uptake, and PEGylation properties. *Chem. Eur. J.* **2010**, *16*, 8329-8339.

(40) Haasnoot, J. G. Mononuclear, oligonuclear and polynuclear metal coordination compounds with 1,2,4-triazole derivatives as ligands. *Coord. Chem. Rev.* **2000**, *200-202*, 131–185.

(41) Ward, M. D. $[Ru(bipy)(CN)_4]^{2-}$ and its derivatives: photophysical properties and its use in photoactive supramolecular assemblies. *Coord. Chem. Rev.* **2006**, *250*, 3128–3141.

(42) King, K. A.; Spellane, P. J.; Watts, R. J. Excited-state properties of a triply ortho-metalated iridium(III) complex. *J. Am. Chem. Soc.* **1985**, *107*, 1431-1432.

(43) Namdas, E. B.; Ruseckas, A.; Samuel, I. D. W.; Lo, S.-C.; Burn, P. L. Photophysics of Fac-Tris(2-Phenylpyridine) Iridium(III) Cored Electroluminescent Dendrimers in Solution and Films *J. Phys. Chem. B* **2004**, *108*, 1570-1577.

(44) Suzuki, K.; Kobayashi, A.; Kaneko, S.; Takehira, K.; Yoshihara, T.; Ishida, H.; Shiina, Y.; Oishi, S.; Tobita, S. Reevaluation of absolute luminescence quantum yields of standard solutions using a spectrometer with an integrating sphere and a back-thinned CCD detector. *PCCP* **2009**, *11*, 9850-9860.

(45) Guardigli, M.; Flamigni, L.; Barigelletti, F.; Richards, C. S. W.; Ward, M. D. Proton Sensitivity of Luminescent $[M(bpy)_2(AB)]^{2+}$ Complexes and Their Monomethylated Counterparts $[M(bpy)_2(ABMe)]^{3+}$ Where AB Is an Asymmetric Quaterpyridine with a Pendant Bipyridyl Site [$M = Ru^{II}, Os^{II}$]. *J. Phys. Chem.* **1996**, *100*, 10620-10628.

(46) Cargill Thompson, A. M. W.; Bardwell, D. A.; Jeffery, J. C.; Rees, L. H.; Ward, M. D. Syntheses, crystal structures, and electrochemical and spectroscopic properties of ruthenium complexes of the N,S-bidentate ligand 2-(2-pyridyl)benzenethiol. *J. Chem. Soc., Dalton Trans.* **1997**, 721-726.

(47) Puckett, C. A.; Ernst, R. J.; Barton, J. K. Exploring the cellular accumulation of metal complexes. *Dalton Trans.* **2010**, *39*, 1159-1170.

(48) You, Y. Phosphorescence bioimaging using cyclometalated Ir(III) complexes. *Curr. Opin. Chem. Biol.* **2013**, *17*, 699-707.

(49) Dunn, K. W.; Kamocka, M. M.; McDonald, J. H. A practical guide to evaluating colocalization in biological microscopy. *Am. J. Physiol. Cell Physiol.* **2011**, *300*, C723-C742.

(50) Bolte, S.; Cordelières, F. P. A guided tour into subcellular colocalization analysis in light microscopy. *J. Microsc.* **2006**, *224*, 213-232.

(51) Sansee, A.; Meksawangwong, S.; Chainok, K.; Franz, K. J.; Gál, M.; Pålsson, L. O.; Puniyan, W.; Traiphol, R.; Pal, R.; Kielar, F. Novel aminoalkyl tris-cyclometalated iridium complexes as cellular stains. *Dalton Trans.* **2016**, *45*, 17420-17430.

(52) He, L.; Li, Y.; Tan, C.-P.; Ye, R.-R.; Chen, M.-H.; Cao, J.-J.; Ji, L.-N.; Mao, Z.-W. Cyclometalated iridium(III) complexes as lysosome-targeted photodynamic anticancer and real-time tracking agents. *Chem. Sci.* **2015**, *6*, 5409-5418.

(53) Ball, G.; Demmerle, J.; Kaufmann, R.; Davis, I.; Dobbie, I. M.; Schermelleh, L. SIMcheck: a Toolbox for Successful Super-resolution Structured Illumination Microscopy *Sci. Rep.* **2015**, *5*, 15915.

(54) Shewring, J. R. *PhD Thesis*, University of Sheffield (UK), **2017**.

(55) Wragg, A.; Gill, M. R.; Hill, C. J.; Su, X.; Meijer, A. J. H. M.; Smythe, C.; Thomas, J. A. Dinuclear osmium(II) probes for high-resolution visualisation of cellular DNA structure using electron microscopy. *Chem. Commun.* **2014**, *50*, 14494-14497.

(56) Tian, X.; Gill, M. R.; Cantón, I.; Thomas, J. A.; Battaglia, G. Live cell luminescence imaging as a function of delivery mechanism. *ChemBioChem* **2011**, *12*, 548-551.

(57) Gill, M. R.; Garcia-Lara, J.; Foster, S. J.; Smythe, C.; Battaglia, G.; Thomas, J. A. A ruthenium(II) polypyridyl complex for direct imaging of DNA structure in living cells. *Nat. Chem.* **2009**, *1*, 662-667.

(58) Zhang, Q.; Tian, X.; Hu, G.; Shi, P.; Wu, J.; Li, S.; Zhou, H.; Jin, B.-K.; Yang, J.; Zhang, S.; Tian, Y. Dual-Functional Analogous cis-Platinum Complex with High Antitumor Activities and Two-Photon Bioimaging. *Biochem.* **2015**, *54*, 2177-2180.

(59) Gill, M. R.; Derrat, H.; Smythe, C. G. W.; Battaglia, G.; Thomas, J. A. Ruthenium(II) Metallo-intercalators: DNA Imaging and Cytotoxicity. *ChemBioChem* **2011**, *12*, 877-880.

(60) de Boer, P.; Hoogenboom, J. P.; Giepmans, B. N. Correlated light and electron microscopy: ultrastructure lights up! *Nat. Meth.* **2015**, *12*, 503-513.

(61) Karreman, M. A.; Hyenne, V.; Schwab, Y.; Goetz, J. G. Intravital Correlative Microscopy: Imaging Life at the Nanoscale. *Trends Cell Biol.* **2016**, *26*, 848-863.

(62) Brown, E.; Verkade, P. The use of markers for correlative light electron microscopy *Protoplasma* **2010**, *244*, 91-97.

(63) De Groot, D. M. D. Comparison of methods for the estimation of the thickness of ultrathin tissue sections. *J. Microsc.* **1988**, *151*, 23-42.

(64) Baggaley, E.; Sazanovich, I. V.; Williams, J. A. G.; Haycock, J. W.; Botchway, S. W.; Weinstein, J. A. Two-photon phosphorescence lifetime imaging of cells and tissues using a long-lived cyclometallated $N_{pyridyl}$^C_{phenyl}^$N_{pyridyl}$ Pt(II) complex. *RSC Adv.* **2014**, *4*, 35003-35008.

(65) Baggaley, E.; Gill, M. R.; Green, N. H.; Turton, D.; Sazanovich, I. V.; Botchway, S. W.; Smythe, C.; Haycock, J. W.; Weinstein, J. A.; Thomas, J. A. Dinuclear ruthenium(II) complexes as two-photon, time-resolved emission microscopy probes for cellular DNA. *Angew. Chem. Int. Ed.* **2014**, *53*, 3367-3371.

(66) Baggaley, E.; Botchway, S. W.; Haycock, J. W.; Morris, H.; Sazanovich, I. V.; Williams, J. A. G.; Weinstein, J. A. Long-lived metal complexes open up microsecond lifetime imaging microscopy under multiphoton excitation: from FLIM to PLIM and beyond. *Chem. Sci.* **2014**, *5*, 879-886.

(67) Ma, X.; Jin, M.; Cai, Y.; Xia, H.; Long, K.; Liu, J.; Yu, Q.; Yuan, J. Mitochondrial electron transport chain complex III is required for antimycin A to inhibit autophagy. *Chem. & Biol.* **2011**, *18*, 1474-1481.

(68) Han, Y. H.; Kim, S. H.; Kim, S. Z.; Park, W. H. Antimycin A as a mitochondria damage agent induces an S phase arrest of the cell cycle in HeLa cells. *Life Sci.* **2008**, *83*, 346-355.

(69) Wragg, A.; Gill, M. R.; McKenzie, L.; Glover, C.; Mowll, R.; Weinstein, J. A.; Su, X.; Smythe, C.; Thomas, J. A. Serum albumin binding inhibits nuclear uptake of luminescent metal-complex-based DNA imaging probes. *Chem. Eur. J.* **2015**, *21*, 11865-11871.

(70) Lo, K. K.-W.; Hui, W.-K.; Chung, C.-K.; Tsang, K. H.-K.; Lee, T. K.-M.; Li, C.-K.; Lau, J. S.-Y.; Ng, D. C.-M. Luminescent transition metal complex biotin conjugates. *Coord. Chem. Rev.* **2006**, *250*, 1724–1736.

(71) Lo, K. K.-W.; Lee, T. K.-M.; Lau, J. S.-Y.; Poon, W.-L.; Cheng, S.-H. Luminescent biological probes derived from ruthenium(II) estradiol polypyridine complexes. *Inorg. Chem.* **2008**, *47,* 200–208.

(72) Sreedharan, S.; Gill, M. R.; Garcia, E.; Saeed, H. K.; Robinson, D.; Byrne, A.; Cadby, A.; Keyes, T. E.; Smythe, C.; Pellett, P.; de la Serna, J. B.; Thomas, J. A. Multimodal super-resolution optical microscopy using a transition-metal based probe provides unprecedented capabilities for imaging both nuclear chromatin and mitochondria. *J. Am. Chem. Soc.* **2017**, *139*, 15907–15913.

Table 1. Photophysical properties of **Ir-L^{pytz}** and **Ir-L^{tol}** in different solvents

Complex	**Solvent**	**Absorption** λ_{max} / nm ($10^{-3}\varepsilon$ / $M^{-1}cm^{-1}$)[a]	**Emission** λ_{max} / nm	ϕ[b]	τ / ns (%)
IrL^{pytz}	H_2O/dmso[c]	385 (6.1), 415 (3.6)	487, 516, 555 (sh)	0.088	550
	CH_2Cl_2	352 (9.9), 390 (5.3), 426 (2.9)	490, 521, 564 (sh)	0.027	290 (15) 99 (85) [d]
	toluene	356 (9.5), 395 (4.4), 431 (2.4)	493, 522, 566 (sh)	0.015	173 (8) 47 (92) [d]
	MeCN	354 (9.5), 392 (5.3), 426 (2.9)	492, 521, 561 (sh)	0.011	157 (10) 45 (90) [d]
Ir-L^{tol}	H_2O/dmso[c]	388 (5.4), 416 (3.3)	484, 515, 555 (sh)	0.055	530
	CH_2Cl_2	359 (10), 395 (5.8), 432 (2.5)	489, 521, 564 (sh)	0.025	186 (11) 89 (89) [d]
	toluene	367 (9.6), 397 (6.1), 433 (2.8)	492, 524, 566 (sh)	0.012	194 (4) 46 (96) [d]
	MeCN	355 (9.7), 394 (5.2), 433 (2.1)	487, 519, 564 (sh)	0.010	188 (4) 46 (96) [d]

a None of the absorption features are clearly-resolved maxima, but rather appear as shoulders on an absorption profile that steadily decreases in intensity at lower energies. Wavelengths and extinction coefficients are therefore approximate.

b Standards used for QY measurements: $[Ir(ppy)_3]$ in aerated Toluene (ϕ = 0.04) (refs. 42, 43); and $[Ru(bpy)_3]Cl_2$ in aerated water (ϕ = 0.042) (ref. 44).

c Complex very poorly soluble in water; solution made by dissolving sample in dmso (0.1 cm^3) and diluting to 100 cm^3 with water.

d Two luminescence lifetime components: see main text.

Table 2. Co-localisation and co-occurrence parameters for Ir-L complexes[a]

Complex	MitoTracker® Orange		CellLight® ER-RFP	
	M	P	M	P
Ir-L^{pytz}	0.91	0.72	0.66	0.38
Ir-L^{tol}	0.96	0.73	0.59	0.29

a M = Manders co-occurrence coefficients, P = Pearson's co-localisation coefficients; see main text

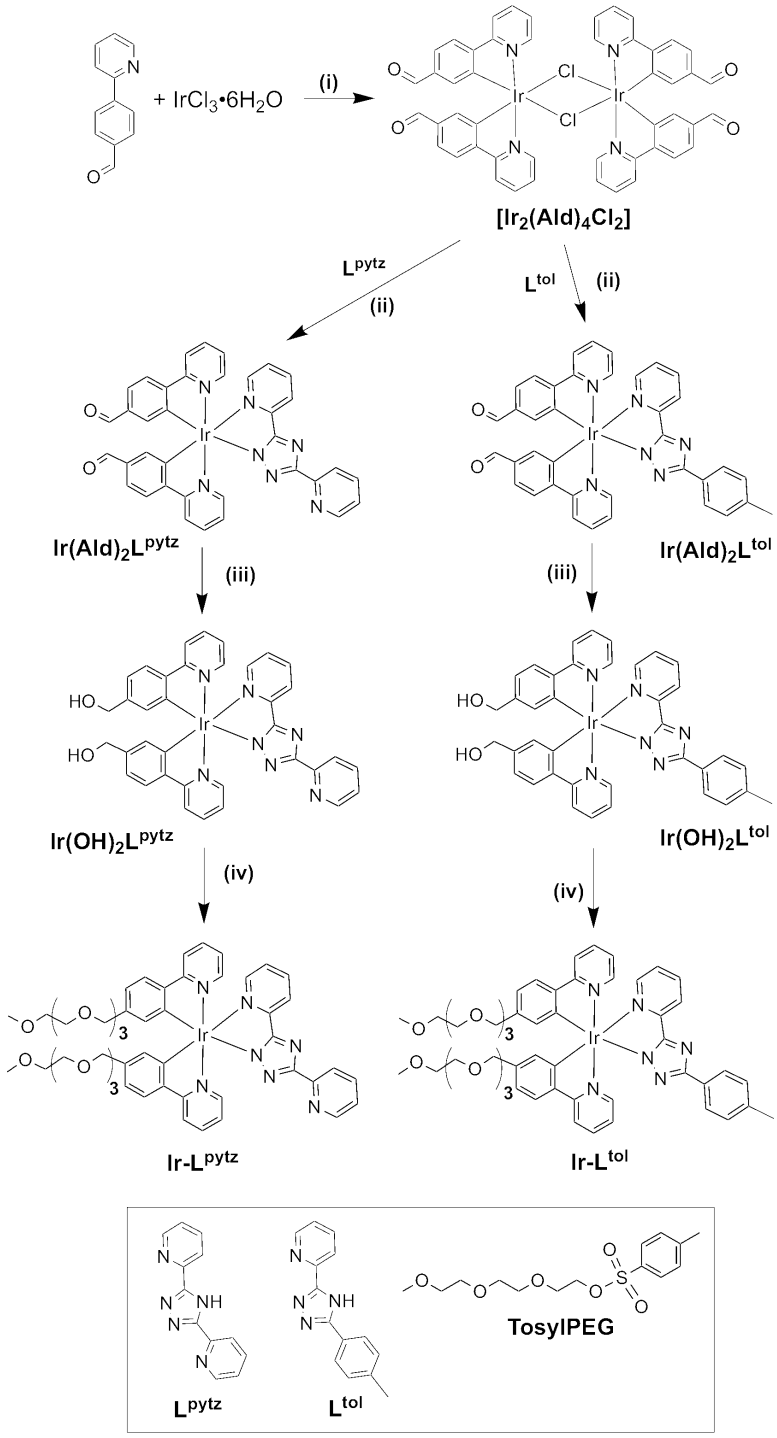

Scheme 1. Synthetic scheme showing preparation of PEG-ylated complexes (**Ir-L^{tol}** and **Ir-L^{pytz}**. (i) 2-Ethoxyethanol/H_2O (3:1), $N_{2(g)}$; (ii) L^n, MeOH/CH_2Cl_2 (2:1), $N_{2(g)}$; (iii) $NaBH_4$, Na_2CO_3, EtOH; (iv) TosylPEG, NaH, THF/DMF (1:1), $N_{2(g)}$.

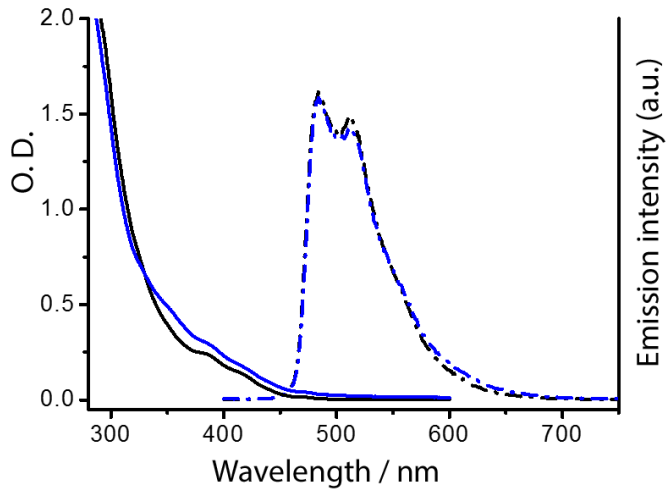

Figure 1. UV-vis (—) and emission (– • –) spectra of **Ir-L^{tol}** (blue) **Ir-L^{pytz}** (black) in H_2O at 5.0 x 10^{-5} M (diluted from a 20 mM stock, 0.3% DMSO).

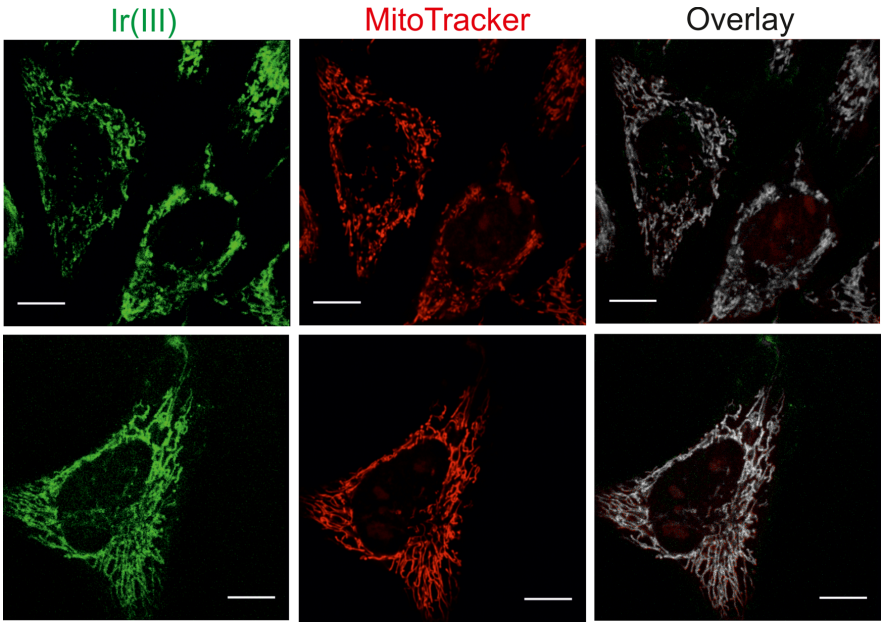

Figure 2. Steady-state confocal images of live HeLa cells co-stained with **Ir-L^{pytz}** (top, 50 μM, 4 hours) and **Ir-L^{tol}** (bottom, 50 μM, 4 hours) and MitoTracker® Orange (200 nM, 35 min). Left: image obtained with Ir(III) emission (λ_{ex} = 405 nm, λ_{em} = 475-575 nm). Middle: image obtained with MitoTracker® orange emission (λ_{ex} = 561 nm, λ_{em} > 590 nm). Right: Overlay image, white pixels depicting co-occurrence of Ir(III) and MitoTracker® emission.

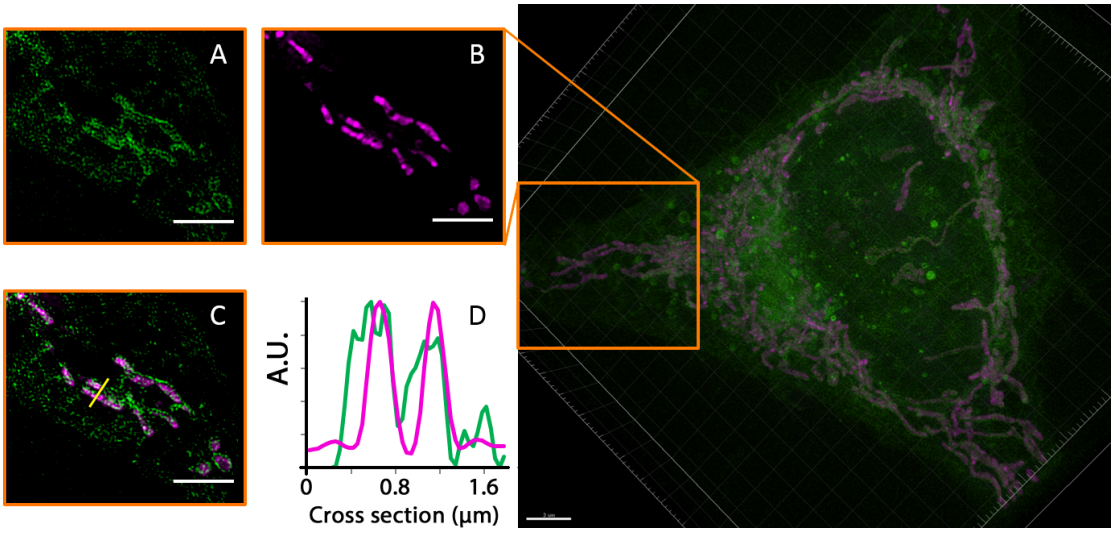

Figure 3. 3D SIM images of HeLa cells treated with **Ir-L^{pytz}** (50 μM, 4 h, green) and MitoTracker® Orange (100 nM, 20 mins, magenta). (A) A single Z-slice displaying emission from **Ir-L^{pytz}**; (B) a single Z-slice displaying emission from MitoTracker® Orange; (C) a single Z-slice displaying overlay of both channels; (D) Emission line profiles along yellow line in (C) overlaid, demonstrating full colocalisation of Ir complex and MitoTracker® Orange; (E) 3D-rendered image of whole cell with emission from both probes (**Ir-L^{pytz}** = green, MitoTracker® Orange = magenta). Scale bars = 3 μm.

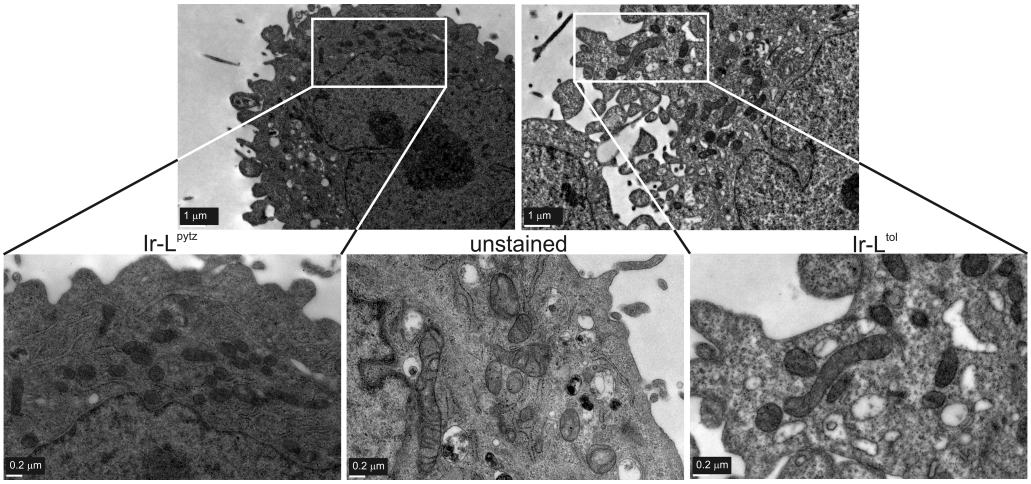

Figure 4. TEM images showing mitochondrial staining of **Ir-L^{pytz}** (left) and **Ir-L^{tol}** (right) at 50 μm compared to an unstained cell (centre). All cells were also treated with contrast agents OsO_4, uranyl acetate (UA) and lead citrate (LC).

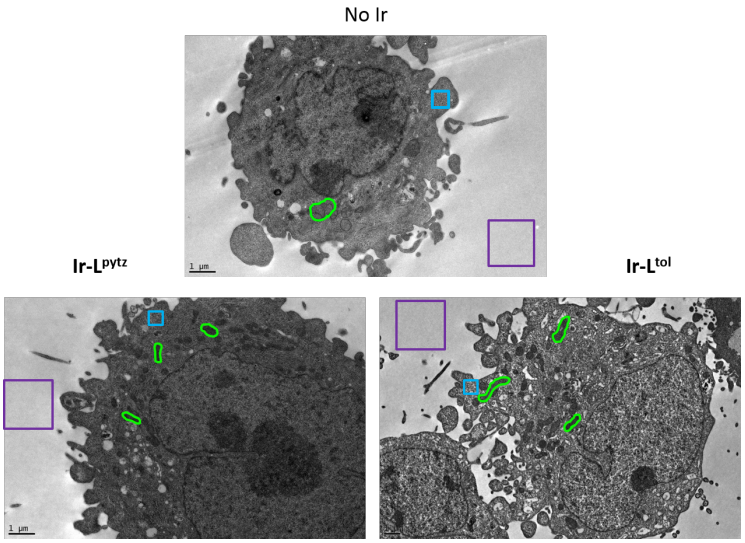

Figure 5. TEM micrographs of HeLa cells showing regions of analysis for relative contrast measurements. Purple box: internal reference (resin only), blue box: cytoplasm, green boxes: mitochondria. Top: control cells (without Ir complex), bottom left: **Ir-L^{pytz}** (50 μm, 4 hr), bottom-right: **Ir-L^{tol}** (50 μm, 4 hr). All cells additionally treated with typical contrast agent OsO_4, LC, UA.

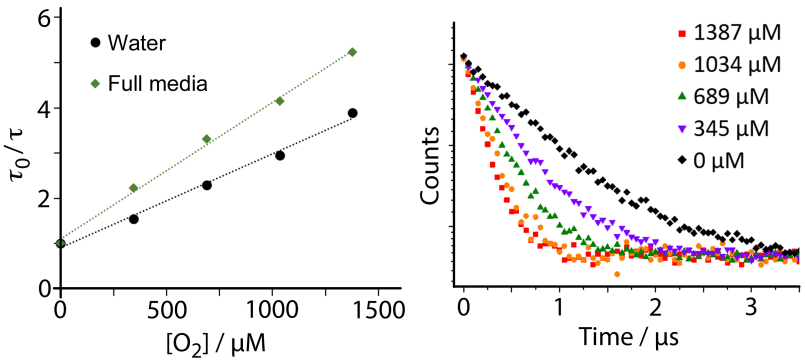

Figure 6. Left: Stern-Volmer plots showing response of **Ir-L^{pytz}** emission lifetime to varying concentrations of O_2 in full cell media (green, $K_{sv} = 3.02 \times 10^{-3}\ \mu M^{-1}$) and water (black, $K_{sv} = 2.08 \times 10^{-3}\ \mu M^{-1}$). Right: Luminescence decay traces of **Ir-L^{pytz}** in water (1.0×10^{-4} M) at varying concentrations of O_2 under two-photon excitation (λ_{ex} = 780 nm).

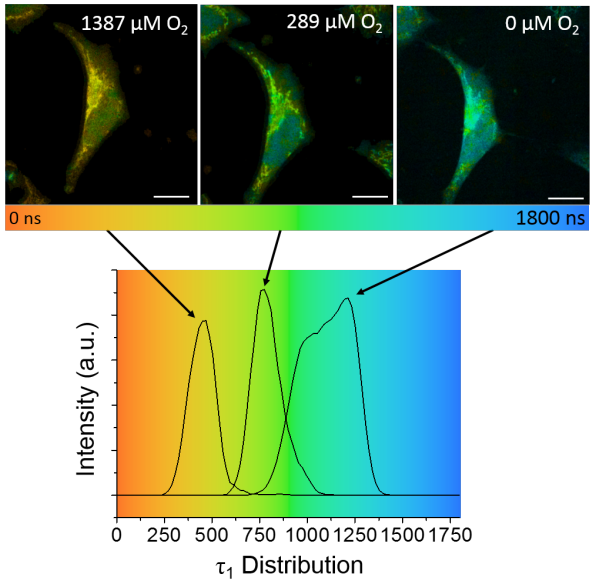

Figure 7. Response of **Ir-L^{pytz}** *in vitro* (50 μM, 4 h) to changing O_2 concentrations using two-photon PLIM (λ_{ex} 760 nm). τ_1 (major component) distributions taken from single cell ROI at each oxygen concentration and plotted on identical rainbow colour chart for comparison. τ_1 distribution maxima: 1387 μM O_2 = 450 ns, 289 μM O_2 = 775 ns, 0 μM O_2 = 1180 ns. Scale bar = 10 μm.

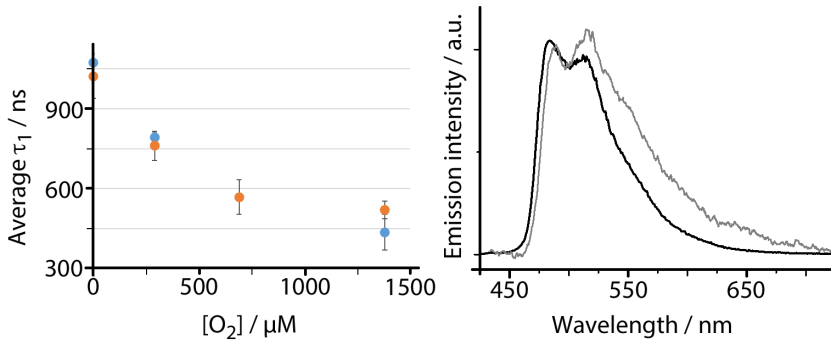

Figure 8. Left: Average emission lifetimes of **Ir-L^{pytz}** in HeLa cells under varying concentrations of O_2. Average mitochondrial lifetimes were calculated from 10 individual data points taken from a FOV. Error bars represent the standard deviation of those 10 data points. Blue circles represent data obtained from one FOV (same cell sample). Orange circles represent data obtained from multiple FOVs (different cell samples). Right: Emission spectra obtained from **Ir-L^{pytz}** in water (black line) under single photon excitation (λ_{ex} = 380 nm) and live cells (grey line) under two-photon excitation (λ_{ex} 760 nm).

SYNOPSIS

A phosphorescent mononuclear Ir(III) complex allows combined confocal microscopy, 3-D superresolution, and transmission electron microscopy imaging of mitochondria – spanning two orders of magnitude in length scales – at the same working concentration, as well as allowing O_2 sensing by lifetime mapping.